1 **A steerable system of RECoverable Autonomous Sonde (RECAS) for**
2 **accessing and studying subglacial lakes**

3 Mikhail A. Sysoev[1], Pavel G. Talalay[1,2], Xiaopeng Fan[1], Nan Zhang[1], Da Gong[1], Yang Yang[1],
4 Ting Wang[1], Zhipeng Deng[1]

5 [1]Institute of Polar Science and Engineering, Jilin University, Changchun, China
6 [2]School of Engineering and Technology, China University of Geosciences, Beijing, China
7 Authors for correspondence: Pavel Talalay, E-mail: ptalalay@yahoo.com; Da Gong, E-mail: gongda@jlu.edu.cn

8

9 **Abstract**

10 The study of subglacial lakes requires clean access and sampling technologies. One of the
11 most promising alternatives is the newly developed thermal drill RECoverable Autonomous Sonde
12 (RECAS), which allows downward and upward ice drilling and subglacial water sampling while
13 the subglacial lake remains isolated from the surface. The original sonde descends downward
14 under the force of gravity, and the borehole trajectory cannot be controlled. However, in certain
15 cases, the sonde would preferably be able to drill at specific angles and directions, enabling it to
16 follow a desired trajectory (e.g., maintaining verticality within the desired range) or bypass
17 obstacles in the ice (e.g., stones and other inclusions). The general principle for the steering
18 RECAS is to adjust the voltage for the electric thermal head heaters, which provides an opportunity
19 to control the heat distribution on the thermal head surface, thereby altering borehole trajectory
20 during drilling. In this paper, the general principles of steering RECAS are described, and
21 experimental results on deviational ice drilling with a controllable electric thermal head are
22 discussed.

23 **Keywords**
24 Ice drilling technology; Subglacial lakes; Clean access sampling; Thermal sonde; Thermal drill;
25 Steerable system

1. Introduction

It is now widely accepted that subglacial hydrological environments are similar to the water distribution found elsewhere on Earth's surface and comprise a vast network of lakes, rivers, and streams located thousands of metres beneath ice caps, glaciers, and the Antarctic and Greenland ice sheets (Bowling et al., 2019; Siegert et al., 2012a; Ashmore et al., 2014). A subglacial lake is considered to be any large body of liquid water existing below an ice mass. The water depth of subglacial lakes varies from a few to several hundred metres (Wright et al., 2011). As of 2022, a total of 773 subglacial lakes have been identified, including 675 in Antarctica, 64 in Greenland, two beneath the Devon Ice Cap, six beneath Iceland's ice caps, and 26 in valley glaciers (Livingstone et al., 2022). The ice thickness above subglacial lakes may vary from several tens to thousands of metres.

Subglacial lakes provide unique information regarding paleoclimatic conditions, basal hydrology, biogeochemical fluxes, and geomorphic activity. It is anticipated that subglacial lakes harbour relict microbial species capable of thriving in complete darkness, low nutrient levels, high water pressures, and isolation from the atmosphere (Skidmore, 2011). In-situ investigations should not contaminate these subglacial aquatic systems. Currently, hot-water drilling systems are considered the cleanest method for accessing subglacial lakes. US teams successfully accessed the Whillans and Mercer subglacial lakes on the coastal margin of West Antarctica in early 2013 and during the 2018-2019 season, demonstrating the well-proven effectiveness of this technology (Priscu et al., 2021; Tulaczyk et al., 2014).

However, access technology using hot-water drilling systems has several significant limitations. For instance, these systems necessitate complicated methods to filter and subject high-speed hot-water flow (>150-200 L/min) to ultraviolet (UV) treatment at the surface. Additionally, they are extremely bulky and highly power-consuming. For example, all drilling and auxiliary equipment for exploring of Subglacial Lake Ellsworth in West Antarctica weighed approximately 60 t, and the fuel supplies weighed a further approximately 55 t (Siegert et al. 2012b). To simplify the drilling process and decontamination of drilling tools, we propose accessing and studying subglacial lakes with a freezing-in electric thermal drill — the RECoverable Autonomous Sonde (RECAS) — capable of downward and upward ice drilling and subglacial water sampling while ensuring that the subglacial lake remains isolated from the surface (Talalay et al., 2014). RECAS is estimated to be 10-20 times less expensive than penetration with a hot-water drilling system, and its installation and operation require only four

specialist staff members (Sun et al., 2023) vs. at least 10 staff required to run a deep hot-water drill (Siegert et al., 2012). The whole RECAS system including sonde, winch, generator, etc. (without fuel supply) weighs about 6.2 t. The sonde surface is thoroughly cleaned before deployment. Although the sonde might drag native microbes, which are embedded in ice, into subglacial targets at various depths as they melt, this occurs in a predictable manner (Schuler et al., 2018). Two concepts similar to RECAS have been proposed by Stone Aerospace, a US engineering company (Pereira et al., 2023; Stone et al., 2018), and Aachen University in Germany (Heinen et al., 2021).

The RECAS was successfully tested in East Antarctica during the 2021-2022 field season, reaching the ice-sheet base at a depth of 200.3 m, sampling basal meltwater and measuring its pressure, temperature, pH, and conductivity before returning to the ice surface (Sun et al., 2023). To expand the sonde's capabilities, we propose equipping it with a steering technique to control and guide the drilling process. This allows drilling at specific angles, depths, and directions, enabling the sonde to follow a desired trajectory (e.g., maintaining verticality within the desired range) or bypass obstacles in the ice (e.g., stones and other inclusions). A similar system was implemented in the IceMole probe (Dachwald et al., 2014). IceMole has an original steering system consisting of a combined thermomechanical drill head and controlled lateral heating. However, the probe is significantly shorter (1 or 2 m in length), has a square cross-section, and can only operate in dry boreholes (maximum drilling depth ~25 m), which differs greatly from the operating conditions of RECAS. Due to the complexity of adapting the IceMole system to RECAS, we developed original steering system. Herein, we describe the general principles of the steering RECAS and discuss the experimental results on deviational ice drilling with a controllable electric thermal head.

2. Steering approaches of the RECAS

2.1. General concept of the steering RECAS

The RECAS comprises four major systems: a heating system (consisting of an upper thermal head, a lower thermal head, and lateral heaters), an inner winch system, a scientific load platform, and a monitoring and control systems (Sun et al., 2024). The upper and lower thermal heads are identical except for the central hole of the cable in the top thermal head (Li et al., 2020). Thus, it can drill both downward and upward and move within the borehole using an inner cable-recoiling mechanism, similar to how a spider climbs on its silk line.

84   Two RECAS prototypes were developed: RECAS-200, with a 200-m-long cable inside, and

85   RECAS-500, with a 500-m-long cable inside. The RECAS-500 design is shown in Fig. 1. The

86   prototypes differed not only in their drilling ability but also in their sizes, power consumption,

87   number of cartridges in the thermal head, etc. (Table 1). In both prototypes, all heaters are supplied

88   simultaneously at the same voltage from a single source.
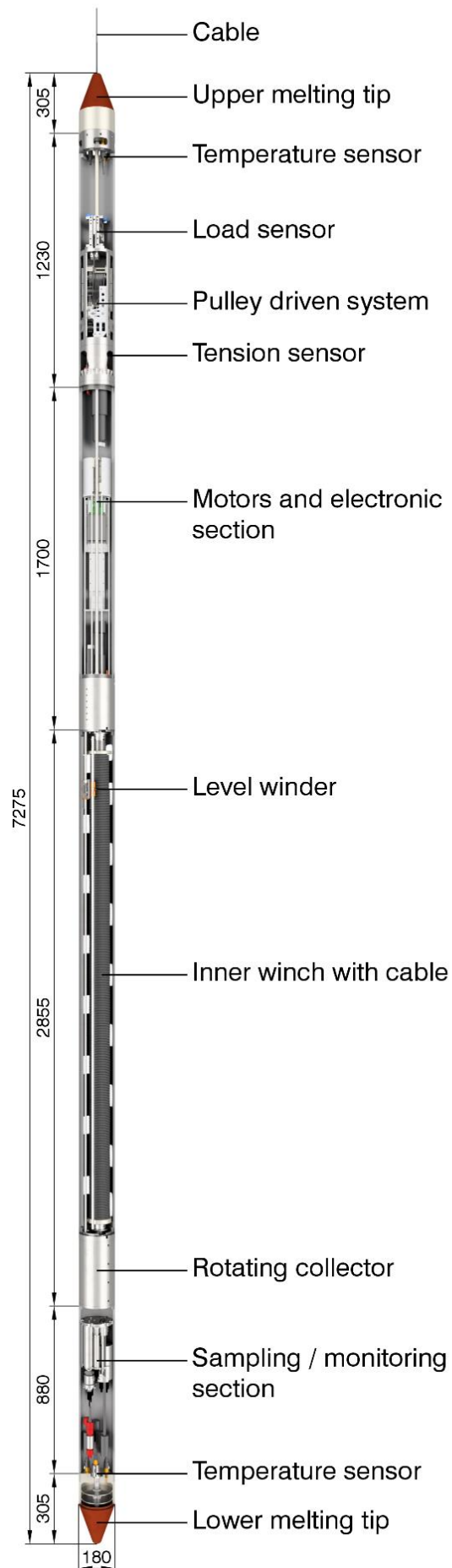
89   **Table 1**

90   General parameters of RECAS-200 and RECAS-500

Prototype	Diameter, mm	Total length, m	Total power, kW	Power of thermal head, kW	Num. of cartridges in thermal head
RECAS-200	160	7.9	8.8	5 nom.; 6 max.	16
RECAS-500	180	7.3	9.7	6.5 nom.; 9.5 max.	20

91   The fundamental principle behind an adjustable electric thermal head is to control the voltage

92   supplied to each pair of adjacent heaters. This enables control over the heat distribution on the

93   thermal head surface and allows borehole deviations during drilling. Furthermore, controlling the

94   heat distribution of the thermal head makes it possible to equalise the load on the heaters as needed.

95   Heating cartridges exhibit variations in their parameters owing to their technological tolerances.

96   Additionally, these parameters may change slightly during long-term use, and heating cartridges

97   can fail because of their long-term use or manufacturing defects.

98   The sonde is steered using data from an inclinometer installed inside it. The data from the

99   inclinometer are transmitted to a personal computer (PC), processed, and converted into pulse-

100   width modulation (PWM) coefficients, which determine the PWM duty cycle for a specified

101   number of channels. In the subsequent tests using the RECAS-200 prototype, the PC will be

102   replaced with a microcontroller mounted inside the sonde. The PMW coefficients are transmitted

103   from the computer to a PWM generator (Sup. 2) inside the sonde prototype, where an individual

104   PWM signal is generated for each channel. Each PWM signal is amplified using a power module

105   (Sup. 3) and supplied to the corresponding heater inside the thermal head. The PWM signal duty

106   cycle limits the heater power.

107   It was decided to implement three control modes: manual mode, where the heaters

108   configuration can be set manually; semi-automatic mode, where the configuration is "linked" to

109   the tilt angle of the sonde; and automatic alignment mode, where the system will "attempt" to align

110   the sonde to a vertical position and/or maintain the sonde vertically.

4

Cable

Upper melting tip

Temperature sensor

Load sensor

Pulley driven system

Tension sensor

Motors and electronic section

Level winder

Inner winch with cable

Rotating collector

Sampling / monitoring section

Temperature sensor

Lower melting tip

305

1230

1700

7275

2855

880

305

180

111

112   **Fig. 1.** General schematic of the RECAS-500 with a 500-m-long cable inside (all dimensions are in mm)

113 *2.2. RECAS positioning estimation*

114   The following method was employed to convert the values received from the inclinometer into

115   PWM coefficients for automatic alignment mode. The inclinometer transmitted deviation values in

116   degrees along the *X* and *Y* axes. As shown in Fig. 2, the *X* and *Y* axes correspond to the inclinometer

117   axes in the horizontal plane. Point *A* indicates a deviation, with $X = 4.5$ and $Y = -3$, for instance.

118   Eight pairs of 16 heaters are shown schematically in the form of circles, designated as *H1-H8*.
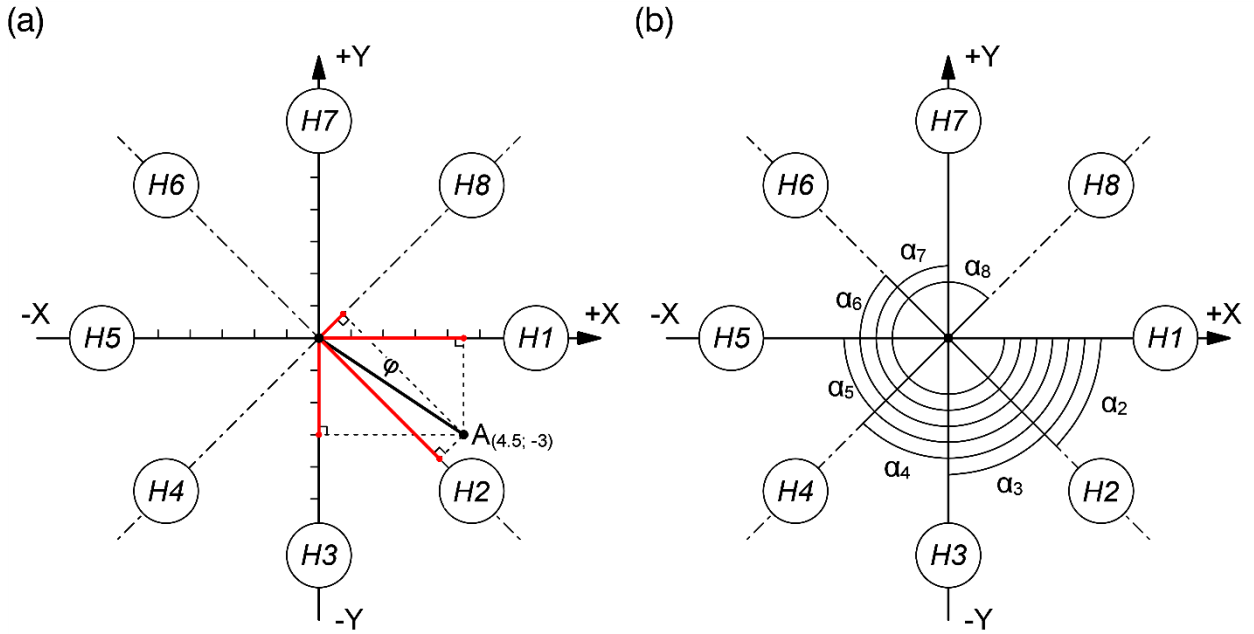
119

120   **Fig. 2.** Schematic diagram of the heater pairs *H1-H8* relative location and inclinometer in the sonde prototype.
121   (a) projection length *l*, (b) heater pair axis angle *α*

122   First, the absolute inclination φ is determined (Eq. 1). This value is required not only for

123   subsequent calculations but also for monitoring purposes.

$$\varphi = \sqrt{X^2 + Y^2} \tag{1}$$

124   where *X* and *Y* are the coordinates received from the inclinometer.

125   Next, the projection length values l_n of φ on the axis of each heater pair are determined as

126   follows (indicated in red in Fig. 2a):

$$l_n = \varphi \cos\left(\arctan\left(\frac{Y}{X}\right) - \alpha_n \right) \tag{2}$$

127   where α_n is the heater pair axis angle relative to the *X* axis (Fig. 2b).

6

128   To obtain the required PWM coefficients, the l_n values must be converted to relative values

129   in the range of 0-1. Additionally, it is necessary to be able to adjust the resulting coefficients. For

130   this purpose, a logistic function (logistic curve) was used (Kyurkchiev et al., 2015). After slight

131   adaptation to meet our conditions, the final equations take the following form:

$$K_n = \frac{1}{1 + \exp(-T(l_n + V))}; \quad V = \frac{1}{T} \ln \frac{-y_{off}}{y_{off} - 1} \tag{3}$$

132   where K_n is the PWM coefficient for each heater pair, V is the intermediate coefficient, T is the

133   correction coefficient (above zero), and y_{off} is the offset coefficient (0-1).

134   T and y_{off} are used to adjust the final values. The coefficient y_{off} limits the maximum average

135   PWM coefficient value (i.e., with zero inclination and $y_{off} = 0.5$, all PWM coefficients will be 0.5).

136   Meanwhile, the correction coefficient T affects the rising section length where the derivative is

137   relatively large. The influence of T and y_{off} on the final results is illustrated by the example

138   discussed next.

139   *2.3. RECAS positioning calculation example*

140   For the calculation example, random inclinometer values are taken as: $X = 4.5$; $Y = -3$. Then,

141   absolute inclination is

142    $\varphi = \sqrt{X^2 + Y^2} = \sqrt{4.5^2 + (-3)^2} = \sqrt{20.25 + 9} = \sqrt{29.25} = 5.41$.

143   The α values for eight heater pairs are presented in Table 2.

144   **Table 2**
145   The α values for eight heater pairs

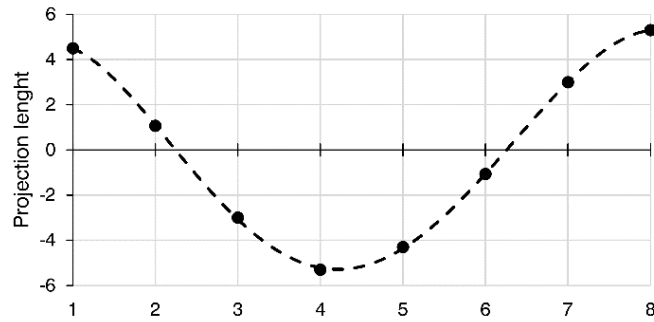| α_1	α_2	α_3	α_4	α_5	α_6	α_7	α_8
0°	45°	90°	135°	180°	225°	270°	315°

146   The projection length of φ for the first heater pair is estimated as

147    $l_1 = \varphi \cos\left(\arctan\left(\frac{Y}{X} \right) - \alpha_1 \right) = 5.41 \cdot \cos\left(\arctan\left(\frac{-3}{4.5} \right) - 0 \right) = 5.41 \cdot \cos(-33.69) = 5.41 \cdot 0.83 = 4.5$.

148   The calculation results for all eight projection length values are listed in Table 3 and shown

149   in graph form in Fig. 3.

7

Table 3

Projection length values

l_1	l_2	l_3	l_4	l_5	l_6	l_7	l_8
4.5	1.06	-3	-5.3	-4.5	-1.06	3	5.3

Fig. 3. Projection length values.

For this example, the following coefficients were selected: $T = 1$ and $y_{off} = 0.8$. Then, the intermediate and PWM coefficients for the first heater pair are

$$V = \frac{1}{T}\ln\frac{-y_{off}}{y_{off}-1} = \frac{1}{1}\cdot\ln\frac{-0.8}{0.8-1} = \ln 4 = 1.39 \, ;$$

$$K_1 = \frac{1}{1+\exp(-T(l_1+V))} = \frac{1}{1+\exp(-1\cdot(4.5+1.39))} = \frac{1}{1+\exp(-5.89)} = \frac{1}{1+0.0028} = 0.997 \, .$$

The results of the final PWM coefficient calculations are listed in Table 4.

Table 4

PWM coefficients

$K1$	$K2$	$K3$	$K4$	$K5$	$K6$	$K7$	$K8$
0,997	0,92	0,17	0,02	0,04	0,58	0,99	0,999

To illustrate how T and y_{off} affect the final PWM coefficients, the calculation results with the same deviation values but different T and y_{off} values are presented in Figs. 4 and 5.
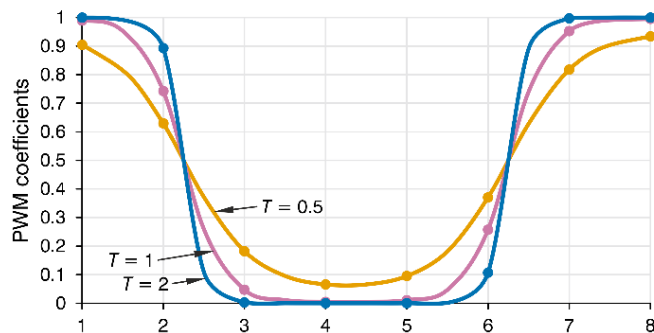
Fig. 4. PWM coefficients at constant $X = 4.5$; $Y = -3$; $y_{off} = 0.5$, and three different values of $T = 0.5$; $T = 1$; $T = 2$.

8
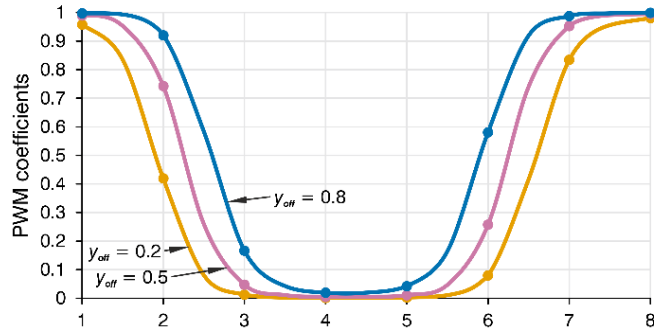
165

166   **Fig. 5.** PWM coefficients at constant $X = 4.5$; $Y = -3$; $T = 1$, and three different values of $y_{off} = 0.2$; $y_{off} = 0.5$; $y_{off} = 0.8$.

167   The coefficients T and y_{off} should be selected experimentally. Therefore, they do not need to

168   remain constant. They may depend on other parameters; for example, y_{off} may depend on the

169   absolute inclination. It is worth noting that when the correction coefficient T approaches zero, all

170   PWM coefficients tend towards the y_{off} value, which means that the heat distribution on the thermal

171   head surface approaches a uniform pattern.

172   **3. Passability of the RECAS**

173   Before changing the borehole trajectory direction, determining the passability of the sonde

174   in the drilled borehole is essential. Owing to its length exceeding 7 m, the RECAS has a high

175   likelihood of becoming stuck in the borehole, even with relatively small deviations. The main

176   parameter affecting sonde passability in a curved borehole is the deviation intensity. To

177   characterise the borehole deviation intensity at a specific interval along its axis, the relative zenith

178   angle values were used, considering the interval between their measurement points. Therefore, the

179   zenith deviation intensity was determined as follows (Zvarygin, 2010; Shamshev et al., 1983):

$$i_\theta = \frac{\Delta\theta}{\Delta L} \tag{4}$$

180   where $\Delta\theta$ is the relative zenith angle in degrees and ΔL is the borehole axis interval length.

181   If the deviation intensity at some borehole interval remains constant ($i_\theta = $ const), it means

182   that the borehole is curved along a circular arc at a certain interval. The borehole radius of

183   curvature R depends on the deviation intensity, as follows (Zvarygin, 2010) (Fig. 6):

$$R = \frac{57.3}{i_\theta} \tag{5}$$

9
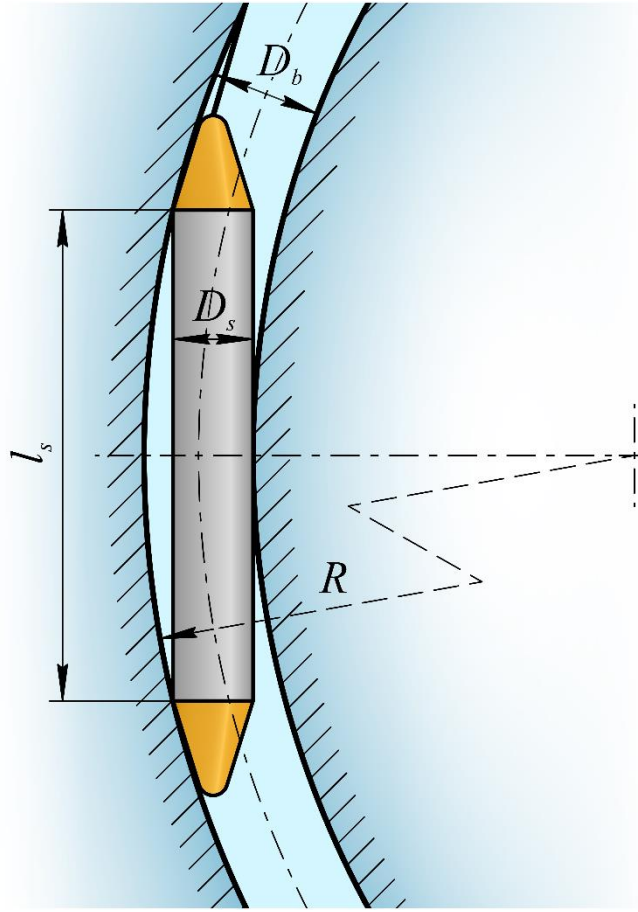
185 **Fig. 6.** Schematic of the stuck sonde in a curved borehole.

186   The passability of a sonde in a borehole interval with known diameter and radius of curvature

187 can be determined as follows:

$$l_s \leq \sqrt{8R\left(D_b - D_s\right) - 4\left(D_s - D_b\right)^2} \tag{6}$$

188 where l_s is the length of the cylindrical part of the sonde (the thermal head length is not included),

189 D_s is the sonde diameter, and D_b is the borehole diameter.

190   As the borehole radius of curvature is considerably larger than the gap between the sonde

191 and borehole diameters, Eq. 6 can be simplified as follows (Shamshev et al., 1983):

$$l_s \leq \sqrt{8R\left(D_b - D_s\right)} \tag{7}$$

192   Based on RECAS field tests, the difference between the borehole and sonde diameters are

193 10-20 mm. This clearance mainly depends on the rate of penetration (ROP), and additional

194 laboratory tests are required to establish a more precise relationship. Considering that the RECAS

195   length is approximately 7 m, the range of radii of curvature ensuring RECAS passibility is in the

196   range of 300-600 m.

197   Therefore, it is not sufficient to simply monitor the borehole inclination to avoid the RECAS

198   from being stuck in the borehole. Instead, it is necessary to continuously estimate the deviation

199   intensity, the borehole radius of curvature, or both at an interval from the bottom hole with a length

200   approximately equal to that of the sonde.

201   **4. Testing stand and sonde prototype design**

202   *4.1. Testing stand*

203   *4.1.1. General testing stand design*

204   The testing stand consists of a sledge, mast, top wheel, winch, and sonde prototype (Fig. 7).

205   All stand parts are mounted on a sledge, which has a modular construction comprising a pair of

206   skis and two welded frames bolted together. A 2-m-high mast is mounted in the middle of the

207   sledge. A small winch is mounted near the mast on a sledge. A block is installed at the top of the

208   mast. The testing stand parameters are listed in Table 5.

209   **Table 5**
210   Testing stand parameters

|	
Mast height	2 m
Max length of the testing sonde	~2 m
Weight of the testing sonde	nom. 100 kg or less; max. 200 kg.
Max. volume of the winch drum	10 m length of 5 mm Kevlar cable
Min. ROP	0.1 m/h (*ROP values refresh rate no more than once per ~6.5 sec*) 0.72 m/h (*ROP values 1 sec. refresh rate*)
Max. possible tripping speed	9.3 m/min (*weight of the testing sonde no more than 57 kg*)
Max. tripping speed	5 m/min (*for 100 kg testing sonde*) 2.3 m/min (*for 200 kg testing sonde*)
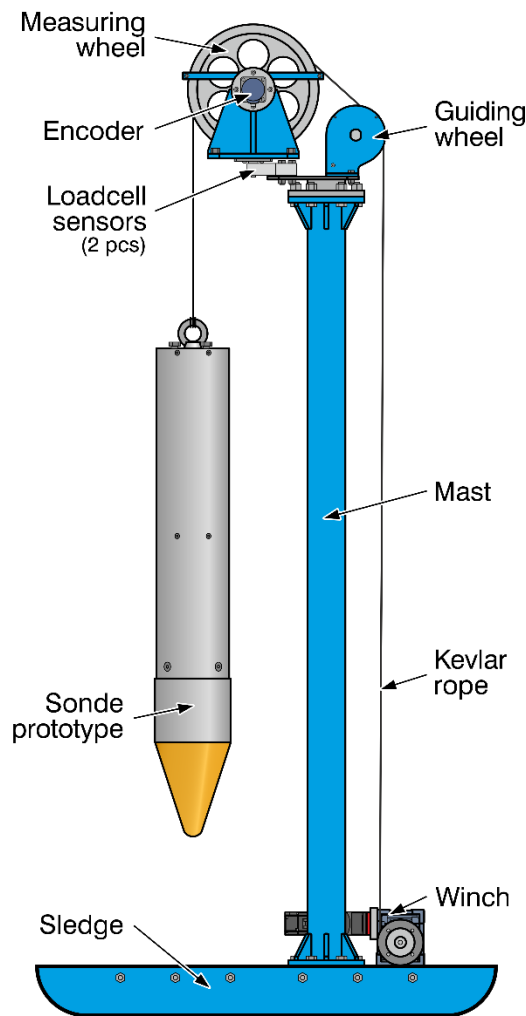
Fig. 7. Schematic of the testing stand

4.1.2. Top block and as-low-as-practicable ROP

      The top block consists of two wheels – a measuring wheel and a guiding wheel, an encoder, and two load-cell sensors. The measuring wheel is designed for a rope with a 5 mm diameter so that the cable length passing through the wheel per revolution equals 1 m ±1 mm. This design simplifies the calculation and further adjustment of the measuring equipment. The guiding wheel is used to guide the rope from the winch to the measuring wheel.

      To register the weight on bit (WOB), two load-cell sensors are installed underneath the measuring wheel assembly. Each sensor can withstand a force of up to 100 daN. To measure the ROP, an encoder with a resolution of 5000 measurements per revolution (MPR) is installed on the measuring wheel shaft. As the ROP is expected to be relatively low, the angular rotation speed of

12

224   the measuring wheel is correspondingly small. Therefore, the higher the encoder resolution, the

225   more frequently it can capture instantaneous low-ROP values.

226   As-low-as-practicable ROP [m/h] can be estimated as follows:

$$\upsilon_{min} = 3600 \cdot \pi \left(D + d \right) n_{min} \tag{8}$$

227   where D is the wheel diameter ($D = 0.3135$ m); d is the rope diameter, and n_{min} is the minimum angular

228   velocity in revolutions per second (RPS)

229   Minimal angular velocity n_{min} is equal to:

$$n_{min} = \frac{1}{tm} \tag{9}$$

230   where m is the encoder resolution in MPR and t is the time after which the data must be updated

231   (in this study, $t = 1$ s).

232   The diameter of the rope axis on the wheel is:

$$D + d = \frac{l}{\pi} \tag{10}$$

233   where l is the rope length passing through the wheel per revolution.

234   After all rearrangements, the as-low-as-practicable ROP is:

$$\upsilon_{min} = 3600 \cdot \frac{l}{tm} \tag{11}$$

235   Therefore, the as-low-as-practicable ROP, which can be measured with a 5000-MPR encoder,

236   1-m wheel circumference, and a measurement frequency of once per second, was 0.72 m/h.

237   *4.1.3. Winch*

238   The winch is based on an RV50 series worm gearbox. For precise winch control, a 200-W

239   power servo drive was chosen in this study. To compensate for the low servo power, a small

240   PX60 series planetary gearbox with a gear ratio of 1:6 was installed between the worm gearbox and

241   servo. The small drum was customised to hold one layer of 5-mm-diameter Kevlar rope with a length

242   of 10 m. To simplify the winch construction, the drum was mounted directly on the output shaft of

243   the worm reducer. Further details regarding the winch construction design are presented in Sup. 1.

244   *4.1.4. Control system*

245   　　The control system consists of a box containing various data acquisition modules (Fig. 8).

246   Data acquisition modules ADAM 4017+ and ADAM 4018+ were used to collect data from the

247   load-cell sensors and thermocouples, respectively. Counter-tachometer module CTA4001A was

248   used to receive and convert signals from the encoder on the measuring wheel. Two MIK-1100

249   modules were connected to voltage and current sensors. Temperature module DT320 was used to

250   monitor the sonde prototype thermal head temperature. All modules, along with the voltage and

251   current sensors, were mounted in a BDH20016 black case. The wiring schematics for all

252   components are shown in Fig. S5.1 (Sup. 5). The sensor parameters are listed in Table 6.
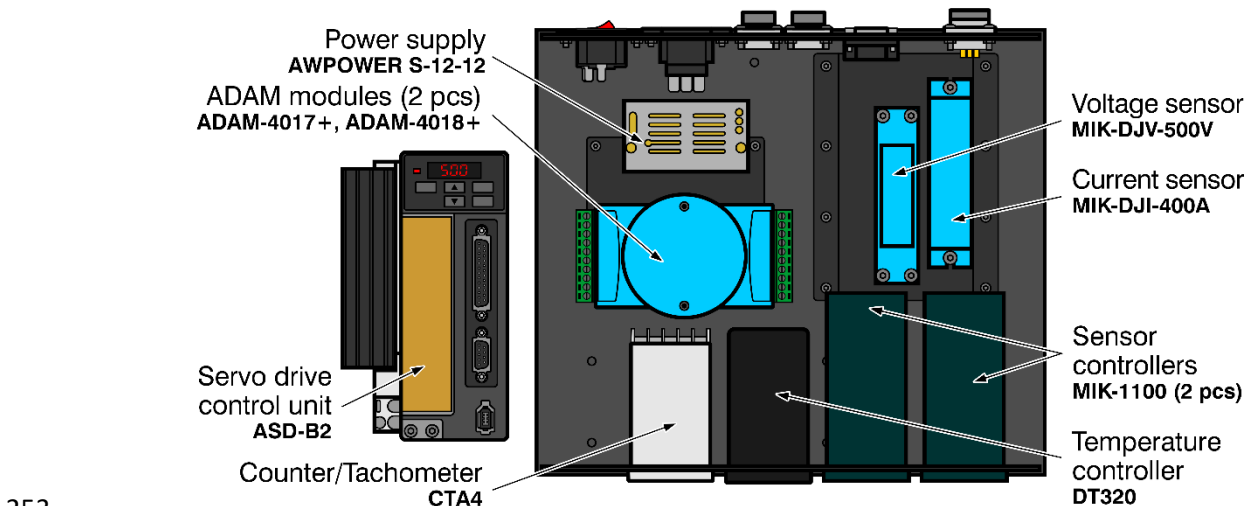
253

254   **Fig. 8.** Schematic of control system

255   **Table 6**

256   Parameters of the sensors

Sensor type	Range	Accuracy	Mounting location	Meas. values
Encoder BC58S10	up to 6000 RPM	5000 MPR	Top block	ROP, Depth
Load-cell YZC-320C (2 pcs)	up to 100 kg	≤±0.02%	Top block	WOB
Voltage sensor MIK-DJV-500V	up to 500V	0.2%	Control system box	Voltage
Current sensor MIK-DJI-400A	up to 400A	1%	Control system box	Current
T type thermocouples	from -270°C up to 370°C	±0.75%	Ice block, air, thermal head and control system box	Temperature

257 **4.1.5. Software**

258 The control system box, servo control unit, and thermal head control unit were connected to

259 a computer via RS-485. The MODBUS RTU communication protocol was used for data

260 transmission. The software registers the following parameters from the sensors connected to the

261 control system box: ROP (m/h) and Depth (m) (Section 2 in Fig. 9); WOB (daN) (Section 3);

262 Current (A), Voltage (V), Power (W), and three temperatures (°C) (Section 5). Through the

263 thermal head control unit, the software allows monitoring of the sonde prototype inclination and

264 heater status and allows selection between manual and automatic modes (Section 4). A control

265 panel for the winch is located at the bottom of the screen (Section 6).


266
267 **Fig. 9.** Software main screen
268

269 *4.2. Testing sonde prototype*

270 *4.2.1. General structure of the sonde prototype*

271 The sonde prototype consisted of a thermal head borrowed from the RECAS-200 prototype

272 and a control unit assembled inside the housing (Fig. 10). The total sonde prototype length was

15

273 approximately 1.1 m, and its weight was approximately 35 kg. The sonde prototype was suspended

274 using a Kevlar rope tied to a hook. Electric lines for the power supply and communication were

275 inserted through isolated connectors in the top cover.
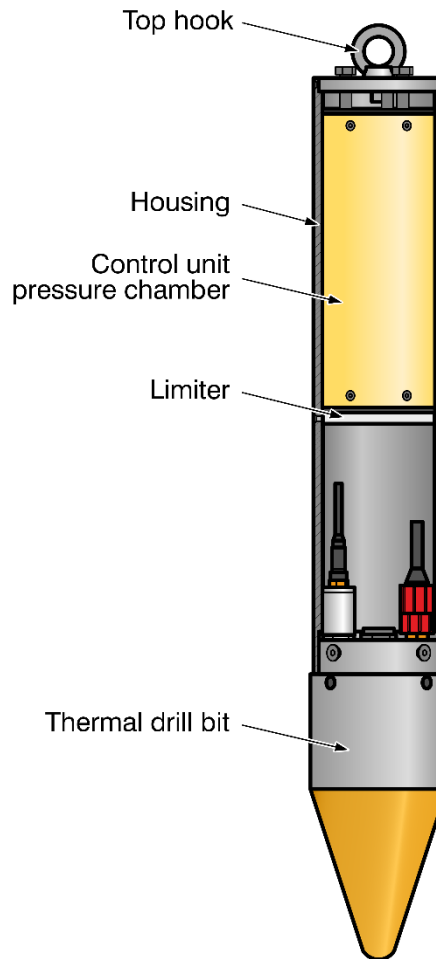
276
277 **Fig. 10.** Schematic of the self-steering sonde prototype
278

279 *4.2.2. Thermal head*

280 The thermal head diameter was 160 mm. It had 16 heat cartridges with a total power of

281 approximately 7.6 kW (Li et al., 2020; Talalay et al., 2019). The heaters connections in the

282 thermal head were redesigned (Fig. 11). Fuses were installed on each heater, and a distribution

283 board was designed to distribute the load and connect it to the power connector (Fig. 12). To allow

284 each heater to be individually connected to a power source, the power connector was also changed

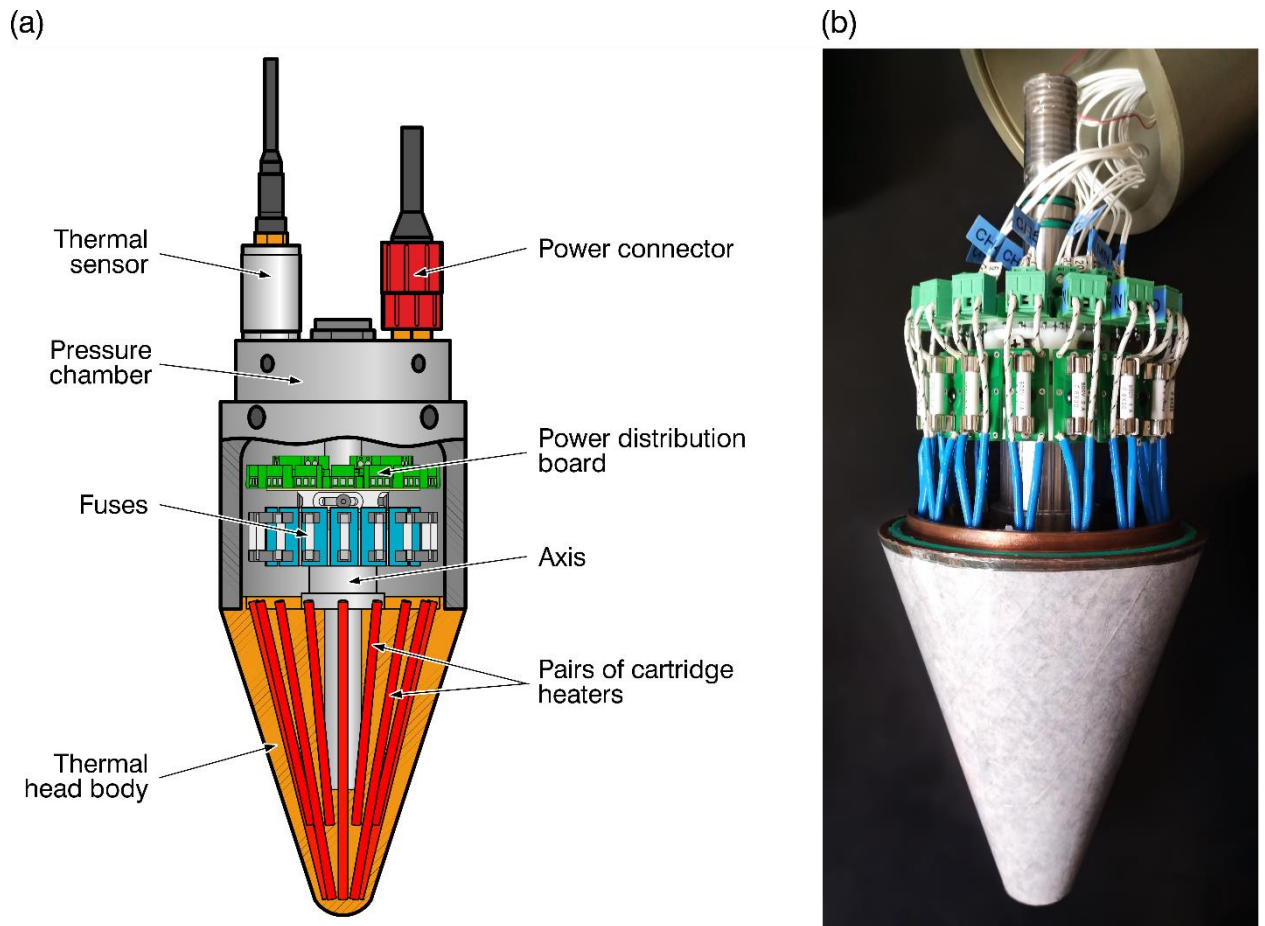285 from two four-pin connectors to one 21-pin connector.

(a)   (b)

Thermal sensor

Power connector

Pressure chamber

Power distribution board

Fuses

Axis

Pairs of cartridge heaters

Thermal head body

Fig. 11. Thermal head: (a) schematic and (b) photo

CH0 - AB   FUSE 4A 500V   A
                            LD-POH-6.200 400V 540W
COM
            FUSE 3A 500V   B
                            LD-POH-6.150 400V 410W

CH1 - CD   FUSE 4A 500V   C
                            LD-POH-6.200 400V 540W
COM
            FUSE 3A 500V   D
                            LD-POH-6.150 400V 410W

CH7 - OP   FUSE 4A 500V   O
                            LD-POH-6.200 400V 540W
COM
            FUSE 3A 500V   P
                            LD-POH-6.150 400V 410W
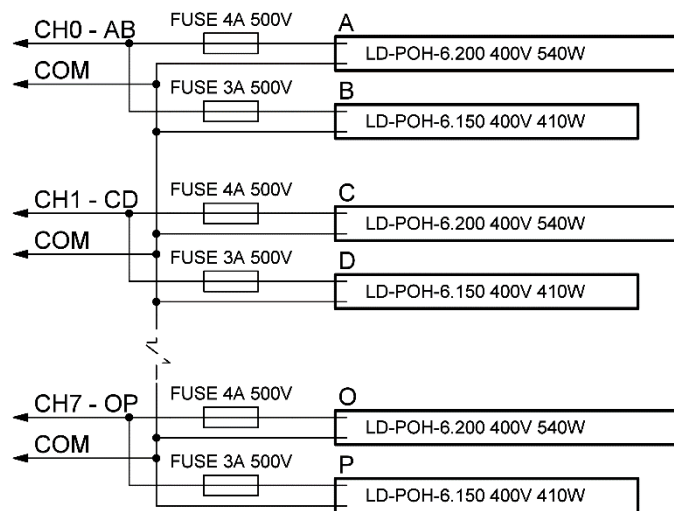
Fig. 12. Electrical schematic of thermal head

The thermal head uses eight long heaters (200 mm in length) and eight short heaters (150 mm in length) that were arranged in an alternating pattern. The cartridges were controlled in pairs, with each long heater paired with an adjacent short one (Fig. 12). Therefore, the number of required PWM signals (PWM channels) was reduced to eight.

295   *4.2.3. Control unit*

296   To control the heaters in the sonde prototype, a control unit was designed as a pressure

297   chamber housing the following components (Fig. 13).
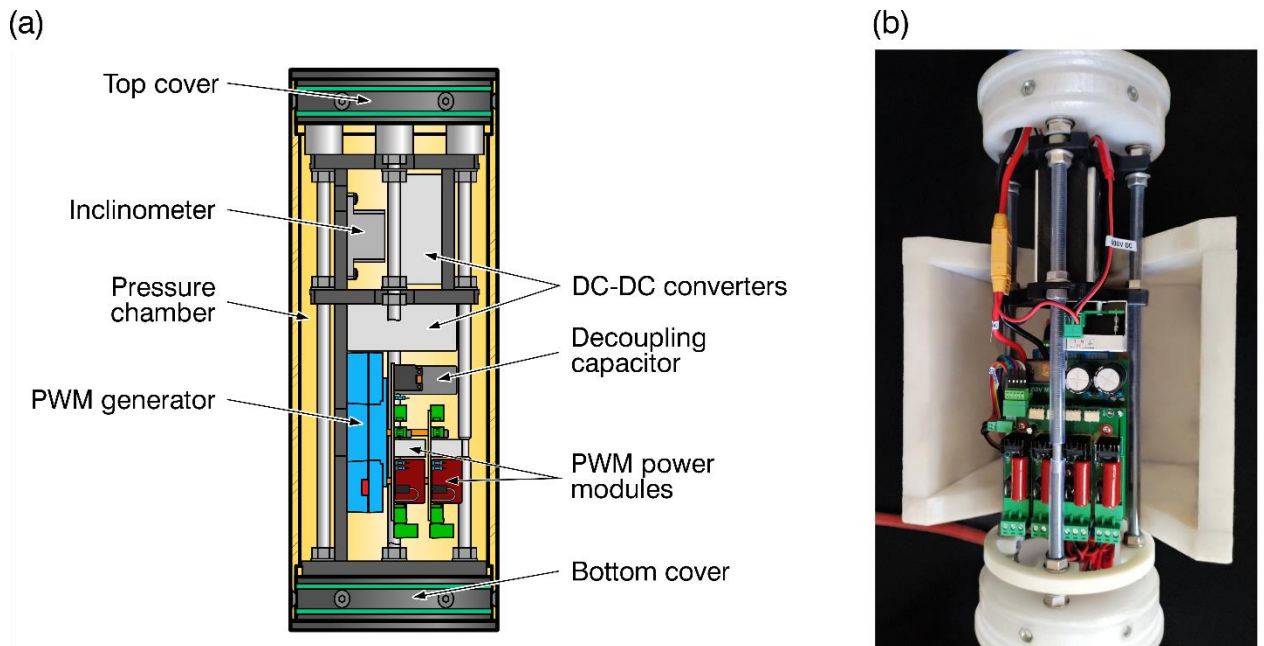
298

299   **Fig. 13.** Control unit: (a) schematic and (b) photo

300   *Dual axis inclinometer*. An inclinometer with two axes was chosen instead of a three-axis one

301   because the control unit was rigidly fixed together with the thermal head inside the sonde prototype,

302   eliminating the need to track the relative rotation along the vertical axis. Also, sonde rotation along

303   the axis will not change the steering direction, because the system constantly calculates new PWM

304   coefficient. The task of tracking the borehole azimuth is planned for future RECAS prototype testing.

305   *PWM generator for 20 channels* (Sup. 2). Although only eight PWM channels were required

306   in this study, the PWM generator was designed with 20 channels to enable the control of individual

307   heaters in the bottom thermal head in the RECAS prototype in the future.

308   *Two power modules, 4 channels each* (Sup. 3). The heater pairs were not connected directly

309   to the PWM generator but through power modules that amplify the corresponding PWM signals

310   from the generator.

311   *Two 15-volt DC-DC converters* (Sup. 4). Two identical DC-DC converters were used to

312   isolate the power supply of the inclinometer and the PWM generator from the power supply of the

313   low-voltage part of the power modules.

314   The wiring schematics for all components are shown in Fig. S5.2 (Sup. 5).

315   All control unit modules, except for the inclinometer, were customised for this study. The

316   primary characteristics of the control units are listed in Table 7.

317   **Table 7**

318   Control unit main parameters

Parameter	Value
Power supply	100-500 V DC
Limit values for angle	X axis ±90
measurement	Y axis ±45°
Angle measuring accuracy	0.2°
Number of PWM channels	8 (upgradeable to 20 Ch.)
Communication with PC	RS-485 MODBUS RTU

319   Further details regarding each individually designed module can be found in the

320   corresponding supplements.

321   **5. Laboratory testing of self-steering sonde prototype**

322   *5.1. Factors and main parameters of experiments*

323   To study the sonde prototype inclination in a drilled borehole, a series of tests were

324   conducted in the Polar Research Center laboratory.

325   The main factors affecting the sonde inclination and drilling performance are:

326   1. Ice temperature (kept constant at −16°C);

327   2. Environmental temperature (varied slightly between +7°C and +12°C);

328   3. ROP, which was controlled by the winch and limited by the power supplied to the heaters

329   inside the thermal head;

330   4. WOB, which changed with the ROP and was limited by the sonde prototype weight.

331   The main parameter to be recorded was the sonde inclination. The sonde inclination was

332   affected by the controlled directional heat distribution on the thermal head surface, which was

333   controlled by limiting the heater power. The control algorithm, with two variable coefficients

334   T and y_{off} is described in Eq. 3. Therefore, the main purpose of the experiments was to determine

335   the dependence of the sonde inclination on these coefficients. For clarity and visual control, blocks

336   of transparent ice with dimensions of $50 \times 50 \times 100$ cm were used in the experiments (Fig. 14).

337
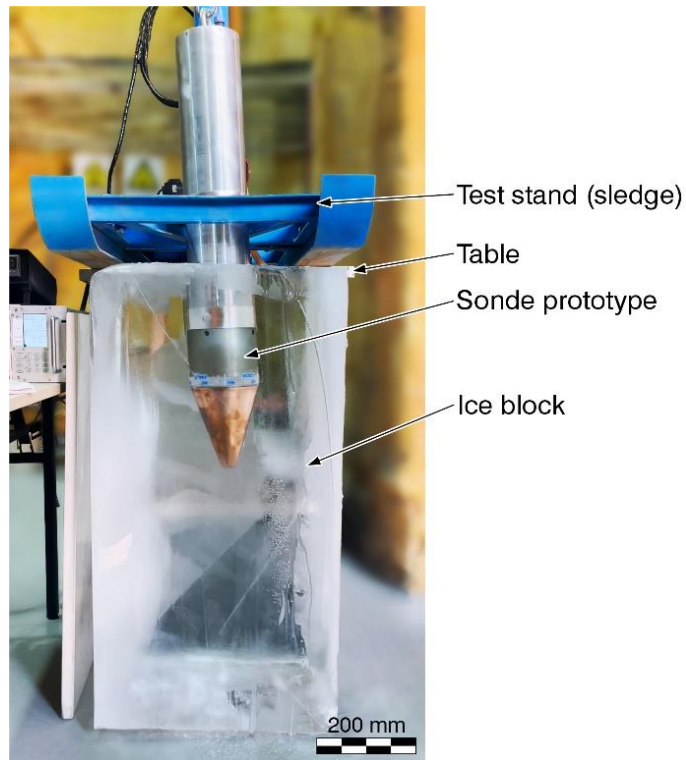
Fig. 14. Testing of the sonde prototype with RECAS-200 controllable thermal head

338
339

340   *5.2. Preliminary experiment*

341   A preliminary experiment was conducted to determine the potential ROP and WOB ranges and

342   the possibility of controlling the sonde prototype inclination in the borehole by regulating the heater

343   power in the thermal head. The experiment recording was divided into four sections (Fig. 15).

344
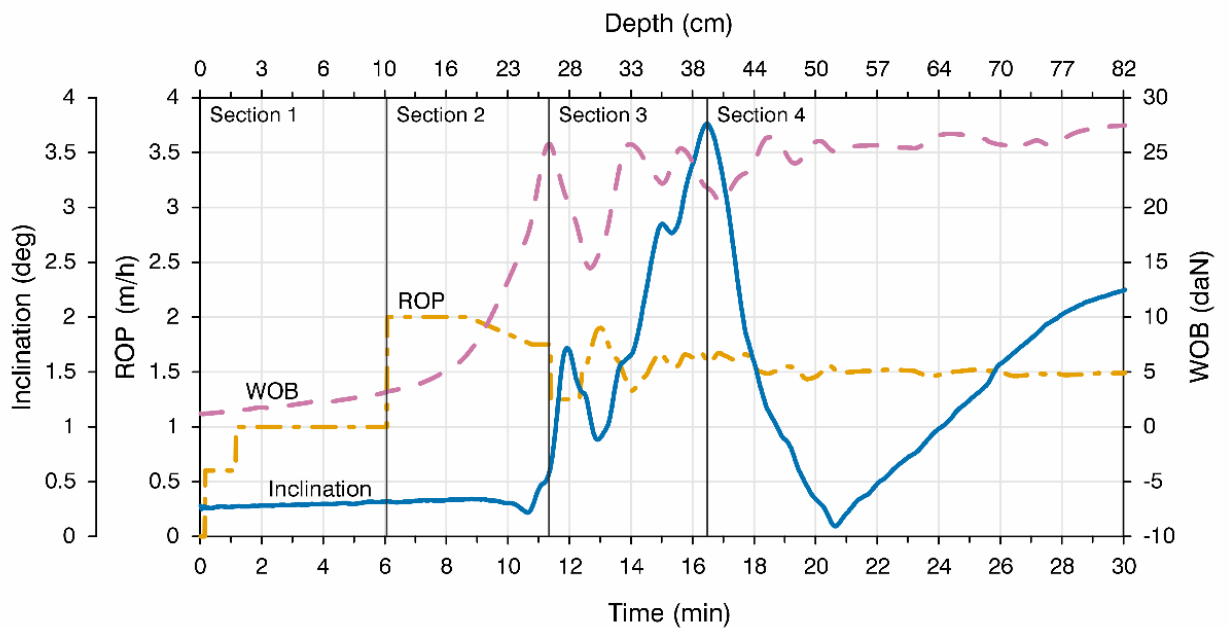
Fig. 15. Recording of the preliminary experiment

345

Section 1 (0-6 min). The first 200 mm of drilling were strictly vertical, with an ROP of 0.6 m/h and all heaters running at 50% power. Subsequently, the power was increased to the maximum, and half of the heaters on one side of the thermal head were switched off. Then, the ROP was increased to 1 m/h.

Section 2 (6-11 min). No sonde prototype inclination was detected, and the ROP was set to 2 m/h to increase the WOB.

Section 3 (12-16 min). The inclination began to increase rapidly when the WOB value reached approximately 25 daN. An attempt was made to stabilise the WOB at this value. The WOB stabilised at approximately 25 daN with an ROP of approximately 1.5 m/h.

Section 4 (16-30 min). When the sonde prototype inclination angle reached approximately 4°, the powered heaters configuration was changed. Four previously powered heater pairs were switched off, and four heater pairs on the opposite side were switched on. The inclination angle decreased to nearly zero and then gradually increased in opposite direction.

Based on the preliminary experimental results, the following conclusions can be drawn. To achieve the desired sonde prototype inclination, the WOB should be approximately 20 daN or higher. However, the test sonde weight was only 35 kg, which significantly reduced the range of the acceptable WOB values. To avoid a situation in which the entire sonde prototype weight would be at the bottom of the borehole, the WOB range was limited to 22-28 daN.

When a 50% power limit was applied, the WOB stabilised at an ROP of approximately 1.5 m/h. Although WOB is not directly controlled, it depends on the ROP. However, constant WOB adjustments via ROP changes using a proportional-integral-derivative (PID) controller were not very effective because the transients significantly influenced the measured parameters. Therefore, in subsequent experiments, we decided to maintain a constant ROP despite potential WOB fluctuations.

Because the coefficient y_{off} limits the maximum average PWM coefficient values, in practice, it limits the power consumption of the thermal head, which, in turn, affects the maximum ROP. Preliminary experimental results showed that testing was meaningful only at WOB values close

21

372   to the maximum. This means that at a certain y_{off} value, it is not possible to change the ROP over

373   a significant range. By analysing the "behaviour" of Eq. 3 we can conclude that at $y_{off} = 0.5$, the

374   heat distribution is the most intense, and the assumed rate of change in borehole trajectory is also

375   at its maximum. The limitation of the maximum borehole depth that can be obtained from the

376   available ice blocks underscores its importance.

377   Based on the above, we conducted a series of experiments with four different correction

378   coefficient T values. The ROP was kept constant at 1.5 m/h. The WOB stabilised between 22 and

379   28 daN. The power consumption was limited to 50% by setting $y_{off} = 0.5$.

380   According to the test plan, in the first approximately 300 mm of each experiment, the sonde

381   prototype should drill with half of the heaters on one side turned off until the sonde inclination

382   angle reaches approximately 4° (Ye et al., 2024). Subsequently, the automatic alignment mode

383   will be enabled. The algorithm will recalculate the PWM coefficients of the heaters at 1-s intervals.

384   It is worth noting that decreasing the PWM coefficient recalculation frequency (i.e., slowing the

385   response to inclination angle changes) can influence the borehole deviation intensity. A decrease

386   in the recalculation frequency is likely to result in a decrease in borehole deviation intensity.

387   *5.3. Experimental results and discution*

388   A total of four experiments were performed. The experimental recordings are shown in

389   Fig. 16. As the values were recorded from the sensors at a frequency of once per second, the graphs

390   are depicted with a 15-value moving-average filter. The graphs show trend lines for each

391   experiment. For each trend line, the bold line indicates the accuracy limits according to the

392   inclinometer specifications (±0.2°).

(a)

(b)

(c)

(d)
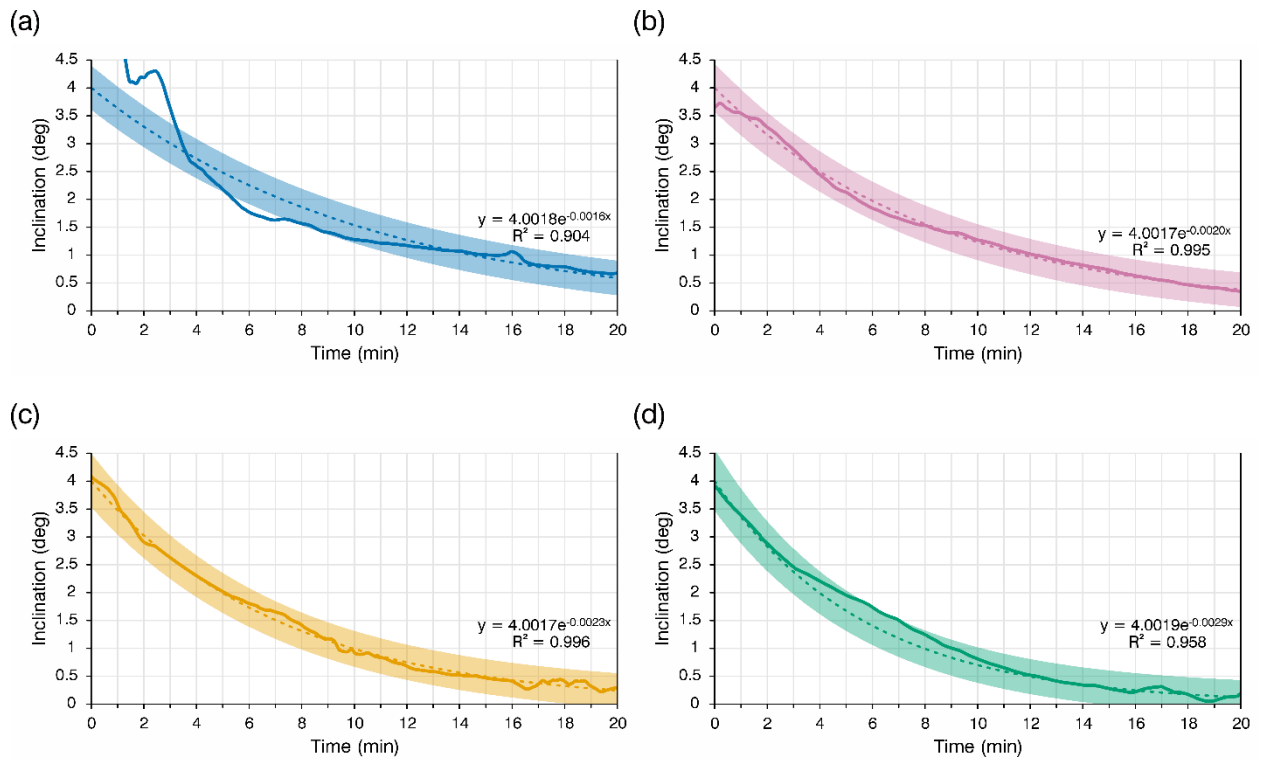
Fig. 16. Recording of the four experiments with trendlines:
(a) Borehole 1, $T = 0.5$, (b) Borehole 2, $T = 1$, (c) Borehole 3, $T = 1.5$ and (d) Borehole 4, $T = 2$

Drilling of borehole 1 with $T = 0.5$ was unsuccessful owing to water leakage from the borehole; consequently, the results were difficult to analyse. The graph illustrates an approximation option intended to be obtained based on the analysis of the other three experiments. The experiment demonstrates that correction coefficient T affected how rapidly the borehole deviation changed over time. For clarity, the approximations of all four experiments are shown in Fig. 17.
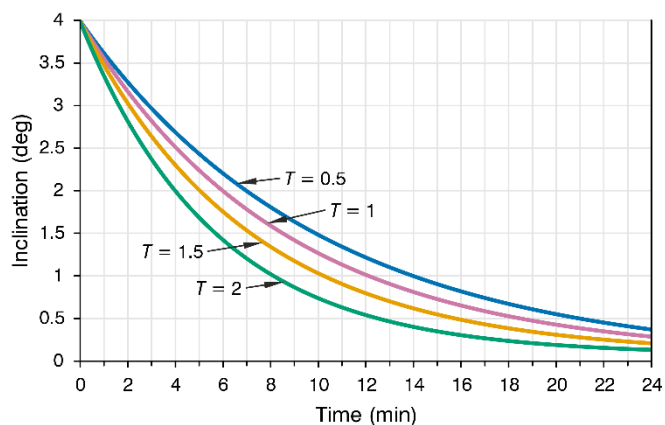

Fig. 17. Approximations of four experiments

To understand how crucial borehole deviations are for the passability of the sonde prototype, it is necessary to analyse the results for the allowable deviation intensity according to the method

405   described in Section 3. In the experiments, the automatic alignment length was

406   approximately 0.5 m. For clarity, it was decided to divide this 0.5-m section of each borehole into

407   several sections, for each of which the radius of curvature was determined. The option of

408   partitioning the path not according to depth but rather according to inclination angle proved to be

409   the most illustrative. Four sections were selected with the following inclination angle ranges:

410   [4°-2.5°], [2.5°-1.5°], [1.5°-1°], and [1°-0.5°].

411   The radius of curvature was determined for all four boreholes in each of the selected sections.

412   To determine the radius, an additional angle (approximately in the middle of the range) was

413   selected. The following additional angle values were selected for further calculations: 3.25° for

414   the range [4°-2.5°], 2° for [2.5°-1.5°], 1.25° for [1.5°-1°], and 0.75° for [1°-0.5°]. Fig. 18 shows

415   the sonde trajectory for the [4°-2.5°] range in borehole 2 ($T = 1$).
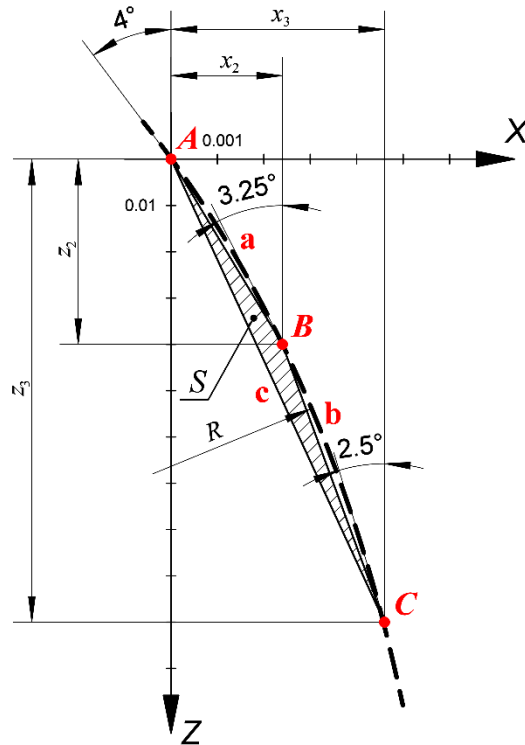
416

417   **Fig. 18.** Borehole 2 ($T = 1$) trajectory within inclination angle range of [4°-2.5°]

418   The sectional radius of curvature was calculated as follows:

$$R = \frac{abc}{4S} \tag{12}$$

419   where a, b and c are the side lengths of triangle ABC and S is the area of triangle ABC.

24

420   The area of the triangle can be determined using Heron's equation:

$$S = \sqrt{p(p-a)(p-b)(p-c)} \qquad (13)$$

421   where p is the semi-perimeter of a triangle.

422   The side lengths of triangle ABC can be determined using the Pythagorean theorem given

423   the coordinates of the points A (x_1, z_1), B (x_2, z_2) and C (x_3, z_3) are known:

$$a = \sqrt{(x_2 - x_1)^2 + (z_2 - z_1)^2} \qquad (14)$$

$$b = \sqrt{(x_3 - x_2)^2 + (z_3 - z_2)^2} \qquad (15)$$

$$c = \sqrt{(x_3 - x_1)^2 + (z_3 - z_1)^2} \qquad (16)$$

424   Knowing the coordinates of points A, B, and C for all sections using Eqs. 12-16, the radius

425   of curvature of each section can be determined. Substituting the radius of curvature into Eq. 6, the

426   maximum allowable sonde length satisfying the passability criteria for each segment can be

427   determined. The resulting radius of curvature and maximum allowable sonde length values are

428   presented in Table 8 and Fig. 19.

429   **Table 8**
430   Radius of curvature and maximum allowable sonde length

Range	Borehole 1, $T = 0.5$		Borehole 2, $T = 1$		Borehole 3, $T = 1.5$		Borehole 4, $T = 2$	
	Radius of curvature (m)	Length of sonde (m)	Radius of curvature (m)	Length of sonde (m)	Radius of curvature (m)	Length of sonde (m)	Radius of curvature (m)	Length of sonde (m)
4°-2.5°	4.701	0.866	3.761	0.775	3.270	0.722	2.594	0.643
2.5°-1.5°	7.64	1.105	6.112	0.988	5.315	0.921	4.215	0.82
1.5°-1°	12.115	1.392	9.692	1.245	8.428	1.161	6.684	1.033
1°-0.5°	20.7	1.819	16.56	1.627	14.4	1.517	11.421	1.351
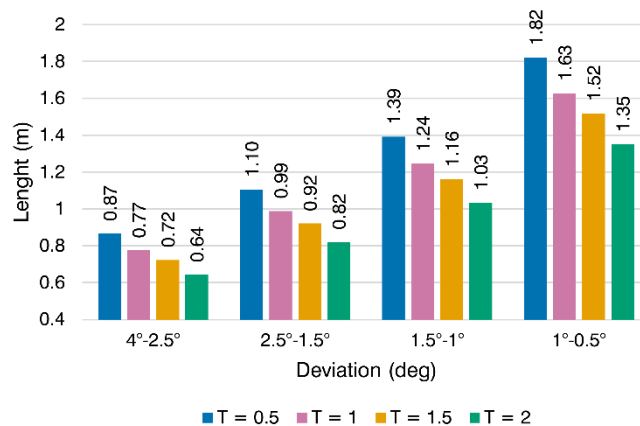
431
432   **Fig. 19.** Dependence of the maximum allowable sonde length at different borehole sections with the same inclination change

25

It is worth noting that the difference between the initial and final angles has a significant impact on the radius of curvature. If the analysed section tends to zero, the radius of curvature of such a section tends to infinity, and vice versa. As a compromise, the ranges were selected to minimise the difference between the size of the deviation angles ranges and the corresponding borehole section lengths.

6. Conclusions

Based on the experimental results for the sonde prototype, the main conclusions of this study can be summarised as follows:

1. The sonde prototype demonstrates a promising potential in controlling the borehole direction and using the RECAS, it should be possible to control the borehole direction to a certain extent using the proposed method.

2. The borehole deviation intensity during drilling can be corrected by controlling the correction coefficient T.

3. It is worth noting that the radius of curvature of a real RECAS would be higher than that obtained experimentally. Further research is required to obtain the RECAS parameters. However, to prevent the RECAS from becoming stuck in its own borehole at the chosen experimental drilling parameters, the borehole deviation radius intensity must be reduced.

4. At the maximum borehole diameter value obtained in the field for the RECAS-200 prototype, the maximum theoretical borehole deviation value cannot exceed 0.67° at a sonde length of approximately 7 m. However, this calculation did not consider the fact that a 7-m-long sonde may exhibit some deformability (especially at the joints), despite its housing being made of stainless steel. At this length, even a small deformation of a few millimetres could positively affect the passability of the sonde in the borehole.

5. Sonde passability at large borehole deviation intensity values can be improved if the housing is structurally divided into several parts capable of deviating from each other (hinged joints).

458   Allowing just a half-degree deviation of one part of the sonde from the other could increase

459   its passability.

460   In future work, we plan to conduct experiments on a larger scale (e.g., with a borehole depth

461   of approximately 10 m) to refine the results in a deviation intensity range closer to that obtained

462   with a real RECAS.

Data availability

464   All raw data can be provided by the corresponding authors upon request.

Author contributions

466   Conceptualization: TPG, SMA, FX; hardware and equipment design: SMA, GD; software

467   development SMA; resources and supplies: FX, GD, DZ, ZN; planning the experiment: SMA, TPG;

468   assistance in preparing for experiments: FX, ZN, GD, DZ; conducting experiments and performed

469   the measurements: SMA, FX; analysing the data: SMA, TPG; project administration: FX, ZN;

470   financial management: YY, WT; supervision TPG; writing the manuscript draft: SMA, TPG;

471   reviewing and editing the manuscript TPG; reviewing the manuscript: FX, GD.

Competing interests

473   The authors declare that they have no conflict of interest.

References

Ashmore, D. W. and Bingham, R. G.: Antarctic subglacial hydrology: current knowledge and future challenges, Antartic science, 26, 758–773, https://doi.org/10.1017/S0954102014000546, 2014.

Bowling, J. S., Livingstone, S. J., Sole, A. J., and Chu, W.: Distribution and dynamics of Greenland subglacial lakes, Nat Commun, 10, 2810, https://doi.org/10.1038/s41467-019-10821-w, 2019.

Dachwald, B., Mikucki, J., Tulaczyk, S., Digel, I., Espe, C., Feldmann, M., Francke, G., Kowalski, J., and Xu, C.: IceMole: a maneuverable probe for clean in situ analysis and sampling of subsurface ice and subglacial aquatic ecosystems, Ann. Glaciol., 55, 14–22, https://doi.org/10.3189/2014AoG65A004, 2014.

Heinen, D., Audehm, J., Becker, F., Boeck, G., Espe, C., Feldmann, M., Francke, G., Friend, P., Haberberger, N., Helbin, K., Nghe, C. T., Stelzig, M., Vossiek, M., Wiebusch, C., and Zierke, S.: The TRIPLE Melting Probe - an Electro-Thermal Drill with a Forefield Reconnaissance System to Access Subglacial Lakes and Oceans, in: OCEANS 2021: San Diego – Porto, San Diego, CA, USA, 1–7, https://doi.org/10.23919/OCEANS44145.2021.9705999, 2021.

Kyurkchiev, N., Markov, S.: Sigmoid Functions: Some Approximation and Modelling Aspects Some Moduli in Programming Environment MATHEMATICA, 1. Aufl., Saarbrücken LAP LAMBERT Academic Publishing 2015, ISBN: 978-3-659-76045-7, 2015.

Li, Y., Talalay, P. G., Sysoev, M. A., Zagorodnov, V. S., Li, X., and Fan, X.: Thermal Heads for Melt Drilling to Subglacial Lakes: Design and Testing, Astrobiology, 20, 142–156, https://doi.org/10.1089/ast.2019.2103, 2020.

Li, X.: Research on the temperature field and closure rate of ice hole formed by thermal drill. Dissertation for the Doctoral Degree. Changchun: Jilin University, 2020.

Livingstone, S. J., Li, Y., Rutishauser, A., Sanderson, R. J., Winter, K., Mikucki, J. A., Björnsson, H., Bowling, J. S., Chu, W., Dow, C. F., Fricker, H. A., McMillan, M., Ng, F. S. L., Ross, N., Siegert, M. J., Siegfried, M., and Sole, A. J.: Subglacial lakes and their changing role in a warming climate, Nat Rev Earth Environ, 3, 106–124, https://doi.org/10.1038/s43017-021-00246-9, 2022.

Pereira, P. V., Durka, M. J., Hogan, B. P., Richmond, K., Smith, M. W. E., Winebrenner, D. P., Elam, W. T., Hockman, B. J., Lopez, A., Tanner, N., Moor, J., Ralston, J., Alexander, M., Zimmerman, W., Flannery, N., Kuhl, W., Wielgosz, S., Cahoy, K. L., Cwik, T. A., and Stone, W. C.: Experimental Validation of Cryobot Thermal Models for the Exploration of Ocean Worlds, Planet. Sci. J., 4, 81, https://doi.org/10.3847/PSJ/acc2b7, 2023.

Priscu, J. C., Kalin, J., Winans, J., Campbell, T., Siegfried, M. R., Skidmore, M., Dore, J. E., Leventer, A., Harwood, D. M., Duling, D., Zook, R., Burnett, J., Gibson, D., Krula, E., Mironov, A., McManis, J., Roberts, G., Rosenheim, B. E., Christner, B. C., Kasic, K., Fricker, H. A., Lyons, W. B., Barker, J., Bowling, M., Collins, B., Davis, C., Gagnon, A., Gardner, C., Gustafson, C., Kim, O.-S., Li, W., Michaud, A., Patterson, M. O., Tranter, M., Venturelli, R., Vick-Majors, T., Elsworth, C., and The SALSA Science Team: Scientific access into Mercer

Subglacial Lake: scientific objectives, drilling operations and initial observations, Ann. Glaciol., 62, 340–352, https://doi.org/10.1017/aog.2021.10, 2021.

Schuler, C. G., Winebrenner, D. P., Elam, W. T., Burnett, J., Boles, B. W., and Mikucki, J. A.: In situ contamination of melt probes: implications for future subglacial microbiological sampling and icy worlds life detection missions, Geol Soc Am., 50, 312–314, https://doi.org/10.1130/abs/2018SE-312314, 2018.

Shamshev, F.A., Tarakanov, C.N., Kudrjashov, B.B., Parijskij, Ju.M., Jakovlev, A.M.: Tehnologija i tehnika razvedochnogo burenija [Technology and technique of exploration drilling]. Moscow, Nedra, 1983 (in Russian).

Siegert, M. J., Woodward, J., Royston-Bishop, G.: Antarctic Subglacial Lakes, in: Encyclopedia of Lakes and Reservoirs, edited by: Bengtsson, L., Herschy, R. W., and Fairbridge, R. W., Springer Netherlands, Dordrecht, 37–39, https://doi.org/10.1007/978-1-4020-4410-6_39, 2012a.

Siegert, M. J., Clarke, R. J., Mowlem, M., Ross, N., Hill, C. S., Tait, A., Hodgson, D., Parnell, J., Tranter, M., Pearce, D., Bentley, M. J., Cockell, C., Tsaloglou, M., Smith, A., Woodward, J., Brito, M. P., and Waugh, E.: Clean access, measurement, and sampling of Ellsworth Subglacial Lake: A method for exploring deep Antarctic subglacial lake environments, Reviews of Geophysics, 50, 2011RG000361, https://doi.org/10.1029/2011RG000361, 2012b.

Skidmore, M.: Microbial communities in Antarctic subglacial aquatic environments, in: Geophysical Monograph Series, vol. 192, edited by: Siegert, M. J., Kennicutt, M. C., and Bindschadler, R. A., American Geophysical Union, Washington, D. C., 61–81, https://doi.org/10.1029/2010GM000995, 2011.

Stone, W., Hogan, B., Siegel, V., Harman, J., Flesher, C., Clark, E., Pradhan, O., Gasiewski, A., Howe, S., and Howe, T.: Project VALKYRIE: Laser-Powered Cryobots and Other Methods for Penetrating Deep Ice on Ocean Worlds, in: Outer Solar System, edited by: Badescu, V. and Zacny, K., Springer International Publishing, Cham, 47–165, https://doi.org/10.1007/978-3-319-73845-1_4, 2018.

Sun, Y., Li, B., Fan, X., Li, Y., Li, G., Yu, H., Li, H., Wang, D., Zhang, N., Gong, D., Wang, R., Li, Y., and Talalay, P. G.: Brief communication: New sonde to unravel the mystery of polar subglacial lakes, The Cryosphere, 17, 1089–1095, https://doi.org/10.5194/tc-17-1089-2023, 2023.

Sun, Y., Pavel, T., Li, Y., Yu, H., Wang, D., Li, G., Xu, L., Gong, D., Wang, J., Wang, J., Wang, T., Zhang, N., Wang, Z., Chen, Y., Liu, Y., Li, Y., Peng, S., Shi, J., An, C., Ge, Q., Xu, J., Ni, X., Cui, Q., Jiang, Q., Mikhail, S., Yang, Y., Wang, R., Wei, X., Wang, Y., Zhu, T., Deng, Z., Alexey, M., Li, B., and Fan, X.: Exploring Antarctic subglacial lakes with RECoverable Autonomous Sonde (RECAS): Design and first field tests, Sci. China Technol. Sci., 67, 1866–1878, https://doi.org/10.1007/s11431-023-2620-3, 2024.

Talalay, P. G., Li, Y., Sysoev, M. A., Hong, J., Li, X., and Fan, X.: Thermal tips for ice hot-point drilling: Experiments and preliminary thermal modeling, Cold Regions Science and Technology, 160, 97–109, https://doi.org/10.1016/j.coldregions.2019.01.015, 2019.

560 Talalay, P. G., Zagorodnov, V. S., Markov, A. N., Sysoev, M. A., and Hong, J.: Recoverable
561   autonomous sonde (RECAS) for environmental exploration of Antarctic subglacial lakes:
562   general concept, Ann. Glaciol., 55, 23–30, https://doi.org/10.3189/2014AoG65A003, 2014.

563 Tulaczyk, S., Mikucki, J. A., Siegfried, M. R., Priscu, J. C., Barcheck, C. G., Beem, L. H.,
564   Behar, A., Burnett, J., Christner, B. C., Fisher, A. T., Fricker, H. A., Mankoff, K. D., Powell,
565   R. D., Rack, F., Sampson, D., Scherer, R. P., Schwartz, S. Y., and The Wissard Science Team:
566   WISSARD at Subglacial Lake Whillans, West Antarctica: scientific operations and initial
567   observations, Ann. Glaciol., 55, 51–58, https://doi.org/10.3189/2014AoG65A009, 2014.

568 Wright, A. and Siegert, M. J.: The identification and physiographical setting of Antarctic
569   subglacial lakes: An update based on recent discoveries, in: Geophysical Monograph Series,
570   vol. 192, edited by: Siegert, M. J., Kennicutt, M. C., and Bindschadler, R. A., American
571   Geophysical Union, Washington, D. C., 9–26, https://doi.org/10.1029/2010GM000933, 2011.

572 Ye, Y., Zierke, S., Li, B., Heinen, D., Li, Y., Wiebusch, C., Kaiser, S., Sun, Y., and Fan, X.:
573   Melting trajectory of the asymmetrically-heated conical thermal head for ice-melting probes, Case
574   Studies in Thermal Engineering, 55, 104160, https://doi.org/10.1016/j.csite.2024.104160, 2024.

575 Zvarygin, V.I.: Burovye stanki i burenie skvazhin [Drilling rigs and well drilling]. Krasnoyarsk,
576   Siberian Federal University, 2010 (in Russian).